Catalysis Today 143 (2009) 286–292

Contents lists available at ScienceDirect

Catalysis Today

journal homepage: www.elsevier.com/locate/cattod

# Cationic (V, Mo, Nb, W) doping of $TiO_2$–anatase: A real alternative for visible light-driven photocatalysts

A. Kubacka [a], G. Colón [b,*], M. Fernández-García [a,**]

[a] Instituto de Catálisis y Petroleoquímica, CSIC, C/Marie Curie s/n, 28049 Madrid, Spain
[b] Instituto de Ciencia de Materiales de Sevilla, Centro Mixto CSIC-Universidad de Sevilla, C/Américo Vespucio 49, 41092 Sevilla, Spain

ARTICLE INFO

*Article history:*
Available online 17 November 2008

*Keywords:*
Photo-catalysis
Binary Ti–M mixed oxides
$TiO_2$
Anatase
Visible and sunlight light absorption and excitation
Pollutant and toluene mineralization and degradation

ABSTRACT

In this article we investigate the structure–activity link of anatase-type Ti–M (M = V, Mo, Nb, and W) mixed oxides used for toluene photo-oxidation under sunlight-type excitation. An analysis of the local and long-range structural and electronic characteristics of the mixed oxides show that only structurally highly homogeneous anatase-type oxides with electronic properties exclusively leading to a band gap decrease drive to efficient visible light-driven photocatalysts. Within our microemulsion preparation method, this only occurs for Ti–V and Ti–W series of samples. The isoelectronic ($V^{4+}$) substitution of $Ti^{4+}$ ions at the anatase lattice is characterized by a low solubility limit (ca. 2.5 at. %), and drives to a limited modification of the band gap and to a moderate enhancement of the photo-activity with respect to bare titania reference systems. W presence at anatase cation positions occurs with concomitant presence of cation vacancies derived by the charge imbalance between the $W^{6+}$ and $Ti^{4+}$ species. A unique W-vacancy local arrangement is detected by the structural characterization, leading to both an important band gap decrease and enhancement of the photo-activity upon sunlight excitation.



## 1. Introduction

$TiO_2$–anatase is by far the most broadly used single-phase photo-catalysts due to its wide availability, modest cost, and low-level toxicity for humans [1]. Prof. Soria group work provides illustrative evidence for the application of $TiO_2$ to gas and liquid phase degradation of pollutants [2,3]. $TiO_2$–anatase is a n-type semiconductor having a wide band gap (3.0–3.4 eV depending on primary particle size and other properties) which necessitates UV light to create energy-rich electron–holes pairs upon absorption. In optical related applications, including all those aiming to use solar light as the energy source, it is desiderable to exploit lower energy photons, extending thus band gap excitations into the visible regime.

The introduction of doping cations into the $TiO_2$–anatase structure to decrease the optical band gap energy is frequently essayed to reach this goal [1,4,5] however this seems a delicate matter as, at the same time, it would be necessary to avoid creation of unwanted charge recombination centers and/or localized electronic states which would prevent an efficient charge separation of excited electron–hole pairs. Additionally, an uncontrolled lowering of the conduction band may place the band edge below the $O_2$ affinity level, jeopardizing the formation of oxygen radicals which are key intermediates in photocatalytic reactions [1]. In spite of these potential problems, to date the most effective way of approaching a continuous and systematic reduction of the $TiO_2$–anatase band gap energy is bringing by doping cations occupying substitutional positions of the network. The theoretical analysis of the substitutional doping shows that the threshold energy of radiation energy absorption decreases proportionally to the number of doping atoms; in fact, for a random distribution of substitutional acceptors/donors of charge, a guassian-type density of states can appear at the upper/lower part of the valence/conduction bands [6]. The corresponding density of states is thus directly proportional to the number of doping ions, giving thus a powerful tool for managing visible light (sunlight) absorption. The trade off upon visible light absorption between the above mentioned potential negative effects derived from the presence of localized electronic states and/or other recombination centers and the positive influence in the band gap energy and subsequent enhancement of the visible-light absorption power is a matter of intense research and essentially an open question. Stress can be put in the fact that such balance is characteristic of sunlight active systems and has no physico-chemical similitude with the

* Corresponding author.
** Corresponding author. Tel.: +34 915854939; fax: +34 915854760.
*E-mail addresses:* gcolon@icmse.csic.es (G. Colón), mfg@icp.csic.es (M. Fernández-García).

0920-5861/$ – see front matter © 2008 Elsevier B.V. All rights reserved.
doi:10.1016/j.cattod.2008.09.028

corresponding balance achieved between positive and negative effects of cation doping upon UV-light excitation.

Substitutional $TiO_2$–anatase-based mixed-metal oxides has been successfully synthesized using Ca, Sr, and Ba [7], V [8–13], Fe [14–16], Cr [9], Zr [17–19], Ta [12,20], Nb [12,13,20,21], Mo [13,22], W [13,23–27], and Sn [28,29]. However, only in the cases of Nb, Mo, W and maybe Zr we expect to fulfill the two primary conditions mentioned above; production of an anatase-type mixed oxide structure with a high-solubility limit (e.g. having a high concentration of doping ions) and a red shifted band gap energy with respect to the parent $TiO_2$–anatase oxide [18,20–25]. For completeness, we have also studied other V/VI group elements like V or Cr as they are frequently used as visible light-driven photocatalysts [8–15] although they may not afford the two mentioned conditions. Nevertheless, in our case we were not able to obtain a dominant anatase-type structure using Cr as doping anion; samples prepared displaying always important quantities of rutile. The remaining cations above mentioned (Ca, Sr, Ba, Fe, Ta, Sn) give band gap energies blue shifted or without shift with respect to the parent $TiO_2$ oxide and are thus inadequate for our purposes. So, here we will summarize our work concerning V, Nb, Mo, and W-doped $TiO_2$-based materials, aiming to establish a structure–photo-activity link able to interpret the chemical properties of these solids in the photodegradation of organic pollutants.

## 2. Experimental

Materials were prepared using a microemulsion preparation method by the addition of titanium tetraisopropoxide to an inverse emulsion containing an aqueous solution (0.5 M) of ammonium metavanadate (Aldrich) or molybdate (Aldrich), hydrated niobium nitrate (Sigma), or ammonium tungsten oxide (Aldrich) dispersed in *n*-heptane, using Triton X-100 (Aldrich) as surfactant and hexanol as cosurfactant [13,23,30]. Water/titanium and water/surfactant molar ratios were, respectively, 18 and 110 for all samples. The resulting mixture was stirred for 24 h, centrifuged, decanted, rinsed with methanol and dried at 298 K for 12 h. Following the microemulsion preparation method, the amorphous Ti–M (M = V, Nb, Mo, W) material was calcined under air for 2 h at 723 K. Samples are named Mn, *n* being the metal atomic content. Reference $TiO_2$, $V_2O_5$, $Nb_2O_5$, $MoO_3$, and $WO_3$ oxides were also synthesized using the same procedure. Table 1 shows the main characterization results for the synthesized materials; Ti:M composition was analyzed by using inductively coupled plasma and atomic absorption (ICP-AAS), while BET surface areas were measured by nitrogen physisorption (Micromeritics ASAP 2010).

Rietveld analysis using the General Structure Analysis Software package (GSAS) was carried out. X-ray diffraction (XRD) patterns were recorded in the range $10^\circ < 2\theta < 120^\circ$ using $0.02^\circ$ steps. X-ray diffraction patterns were obtained using a Siemens D-501 diffractometer with Ni filter and graphite monochromator with a Cu Kα X-ray source. Peak shapes were quantified by a pseudo-Voigt function. Background intensities were described by a cosine Fourier series with 10 coefficients. Each structural model was refined to convergence, with the best result selected on the basis of agreement factors and stability of the refinement. In the last cycle of the refinements, all parameters were varied including scale factor, zero shift, peak shape parameter, half width and lattice parameters. Particle sizes reported in Table 1 were calculated from XRD patterns using the Willianson–Hall method which takes into account the strain and particle size contributions to the XRD peak broadening [31].

UV–visible transmission experiments were performed with a UV-Vis Varian 2300 apparatus. Band gap analysis for an indirect/direct semiconductor was done following standard procedures; e.g. plotting $(h\nu a)^n$ ($n = 1/2$ or 2 for indirect or direct semiconductor; $h\nu$ = excitation energy, $a$ = absorption coefficient) vs. energy and obtaining the corresponding tangent value for null absorption [5]. Raman data were acquired using a Renishaw Dispersive system 1000, equipped with a single monochromator, a holographic Notch filter, and a cooled TCD. Samples were excited using the 514 nm Ar line. XPS data were recorded on 4 mm × 4 mm pellets, 0.5 mm thick, prepared by gently pressing the powdered materials which were outgassed in the prechamber of the instrument at 150 °C up to a pressure below $2 \times 10^{-8}$ Torr to remove chemisorbed water from their surfaces. The Leibold-Heraeus LHS10 spectrometer main chamber, working at a pressure $<2 \times 10^{-9}$ Torr, was equipped with an EA-200 MCD hemispherical electron analyzer with a dual X-ray source working with Al Kα ($h\nu$ = 1486.6 eV) at 120 W, 30 mA. C 1s was used as energy reference (284.6 eV).

XAS (X-ray Absorption Spectroscopy) data were recorded at beamline BM-29 of the ESRF synchrotron (Grenoble, France) using a Si(1 1 1) monochromator detuned at 50% intensity. Three ionization chambers filled with $N_2/O_2$ and a Ti/W foil located between the second and the third ionization chamber were also used. A He cryostat was utilized to obtain EXAFS spectra from samples at 35 K. W–O phase and amplitude functions were extracted from a home-prepared $Cr_2WO_6$ compound (with purity checking by XRD) which displays a nearly octahedral W–O coordination for the first shell with an average distance of 1.92 Å. The $Cr_2WO_6$ reference was prepared by following the method of Krustev [32] W–Ti phase and amplitude functions were extracted from FEFF8.0 calculations modeling an anatase-type structure by using a $Ti_8W_2O_{14}$ cluster, having two W ions bridged by one cation vacancy to achieve electroneutrality. The model includes all Ti/W/vacancy first neighbor atoms of the W/vacancy centers. The goodness of FEFF8.0 calculations for analyzing phase and amplitude functions was tested by simulating the $Cr_2WO_6$

**Table 1**
Main characteristics of the Ti–M materials.

| Sample | M atomic percentage (%)[a] | BET surface area ($m^2\ g^{-1}$) | Size (nm)[b] |
|---|---|---|---|
| $TiO_2$ | – | 106 | 13.3 |
| Ti–V | | | |
| V0.6 | 0.6 | 65 | 8.9 |
| V1 | 1.2 | 66 | 8.1 |
| V2.5 | 2.5 | 60 | 8.5 |
| V5 | 4.9 | 60 | 14.0 |
| V8 | 8.1 | 48 | 12.3 |
| V18 | 18.2 | 33 | 13.2 |
| Ti–Nb | | | |
| Nb10 | 9.7 | 112 | 8.8 |
| Nb20 | 20.2 | 125 | 10.8 |
| Ti–Mo | | | |
| Mo8 | 7.9 | 130 | 8.1 |
| Mo12 | 12.3 | 144 | 6.6 |
| Mo26 | 26.2 | 77 | 5.7 |
| Ti–W | | | |
| W2 | 1.8 | 116 | 11.6 |
| W4 | 3.7 | 111 | 12.0 |
| W11 | 10.9 | 106 | 9.4 |
| W14 | 13.8 | 108 | 10.7 |
| W19 | 19.3 | 122 | 7.9 |
| W20 | 20.4 | 101 | –[c] |
| W27 | 27.0 | 87 | –[c] |

[a] Cation basis (100 × W/(W + Ti)) by ICP-AAS.
[b] For anatase-type structure using XRD and the Willianson–Hall method.
[c] Not measured with confidence.

experimental spectrum. Fitting results were obtained by using the VIPER program (www.dessy.de/klmn/viper.html) [33] and error bars were estimated with $k^1/k^3$ weighted fittings.

Activity and selectivity for the gas-phase photo-oxidation of toluene were tested in a continuous flow annular photoreactor (described elsewhere—Ref. [34]) containing ca. 30 mg of photocatalyst as a thin layer coating on a pyrex tube. The corresponding amount of catalyst was suspended in 1 ml of water, painted on a pyrex tube (cut off at ca. 290 nm) and dried at RT. The reacting mixture (100 ml/min) was prepared by injecting toluene (Panreac, spectroscopic grade) into a wet (ca. 75% relative humidity, RH) 20 vol. % $O_2/N_2$ flow before entering at room temperature to the photoreactor, yielding an organic inlet concentration of ca. 800 ppmv. Under such conditions, the reaction rate is zero order with respect to the total flow and hydrocarbon/oxygen concentrations. After flowing the mixture for 1 h (control test) in the dark, the catalyst was irradiated by four fluorescent daylight lamps (6W, Sylvania F6W/D) with a radiation spectrum simulating sunlight (UV content of 3%), symmetrically positioned outside the photoreactor. Reference experiments with UV lamps (Sylvana F6WBLT-65; 6W, max. at ca. 350 nm) were run using the same reaction set-up and procedure. Reaction rates were evaluated (vide supra) under steady state conditions, typically achieved after 3–4 h from the irradiation starting. No change in activity was detected for all samples within the next 6 h. The concentration of reactants and products was analyzed using an on-line gas chromatograph (HP G1800C) equipped with a HP5 capillary column (0.25 mm I.D. × 30 m) and a flame ionization detector using a SIM mode.

## 3. Results and discussion

In Fig. 1 we plot the activity of Ti–M samples in the photocatalytic degradation of toluene under sunlight excitation. Only $CO_2$ (major product responsible of ca. 75–95% of selectivity) and benzaldehyde were detected as gas-phase products during reaction. Fig. 1 also includes data concerning the microemulsion prepared $TiO_2$ reference and the (anatase + rutile) P25 (Degussa) material. Visual inspection of this figure gives evidence that the reaction rate displays three well differentiated behaviors as a function of the M content of the Ti–M material. The V, Mo, Nb, and W single oxides display very low activity and are not included in this figure. For Ti–V, it shows a maximum located between 2.5 and 5 at. % and practically null activity afterwards. As can be seen in Fig. 1 and has been reported elsewhere, Ti–W samples having a W content above the solubility limit show a decrease of the reaction rate with respect to the W19 sample [23]. The Ti–Mo and Ti–Nb systems show weak dependencies with the heteroatom content although in the first case seems to present better activity as the Mo content grows. The overall maximum of photo-activity is obtained with the W19 sample, with an enhancement factor of 3.3/4.1 times with respect to the "home made" $TiO_2$/P25 references. Local maxima of the Ti–V and Ti–Mo series correspond to the V2.5 and Mo26 samples, respectively, displaying 2.3/2.7 and 1.8/2.2 enhancement factors. Samples show stable reaction rates for about 10 h but prolonged reaction test would be needed to study the long-term stability of these systems. The selectivity for toluene total oxidation (e.g. $CO_2$ product) is approximately constant in the Ti–Nb (ca. 75–80%), Ti–Mo (ca. 95%), and Ti–W (ca. 85%) cases and for Ti–V materials with a V content below or equal to 2.5 at.% (ca. 95%), decreasing for samples having higher loadings (ca. 80%). Experiments under UV excitation (not shown) with selected samples provide evidence that only for Ti–W we obtained a small enhancement of the reaction ratio, well below that obtained using sunlight excitation. This indicates that surface chemistry plays a role on the Ti–W activity upon sunlight excitation but also that this factor has a moderate importance to explain the observed enhancement of the reaction rate with respect to $TiO_2$ reference systems. Non-negative (with respect to the $TiO_2$ reference) and essentially constant values are observed for Ti–V, while negative (Ti–Mo) and rather negative (Ti–Nb) results are observed in the remaining cases.

Fig. 2 exemplifies with the Ti–W case the fact that XRD patterns of all samples show the dominant presence of the anatase-type polymorph (JPCDS 84-1286) and a minor contribution (ca. 10 wt.%) with brookite structure. A study of the M heteroatom solubility limits at the anatase structure was performed using XPS (Fig. 3) and Raman (Fig. 4). A different degree of mixing as a function of the M nature can be expected. In the case of V, it is well known the relatively low solubility limit, associated with the limited stability of $V^{4+}$ species at substitutional positions [8,10,11]. Samples above 1–3 at.% (depending on the synthesis procedure) always display the presence of $V^{5+}$ cations which are associated to surface positions [35] and are clearly detected here using XPS. The binding energies reported in Table 2 show the presence of both $V^{4+}/V^{5+}$ species for the Ti–V specimens [36] with a growth of the fully oxidized chemical state in parallel with the V content. The $V^{5+}$ species seems to dominate in our case for the V5 sample, indicating a solubility limit approaching 2.5 at.%. The presence of $V^{4+}$ species

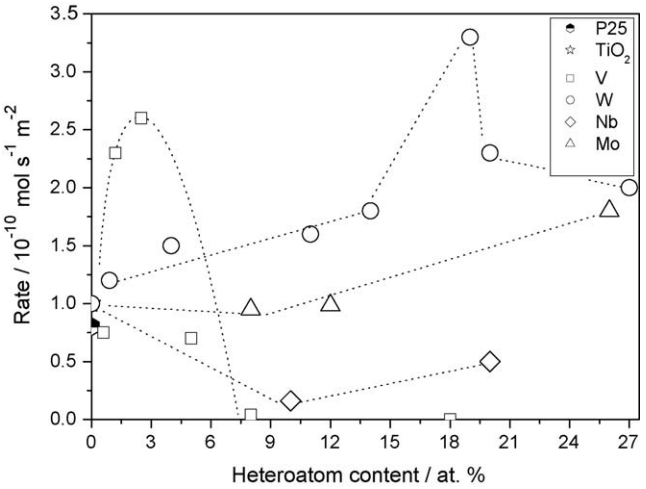


**Fig. 1.** Reaction rates for toluene photo-degradation under sunlight-type excitation using Ti–M samples.

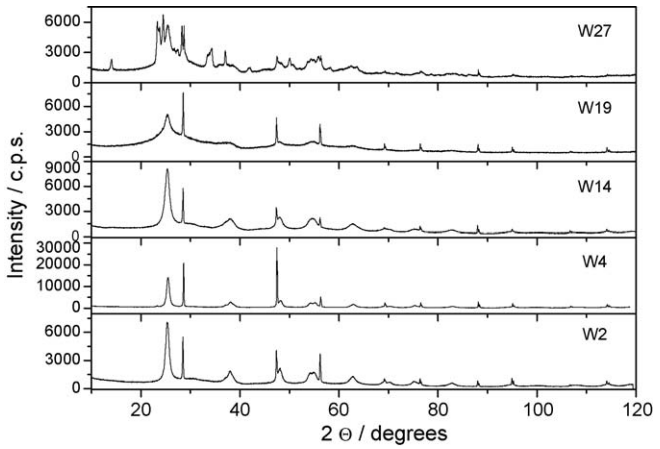


**Fig. 2.** XRD patterns for selected Ti–W samples. Narrow peaks come from a Si internal reference.

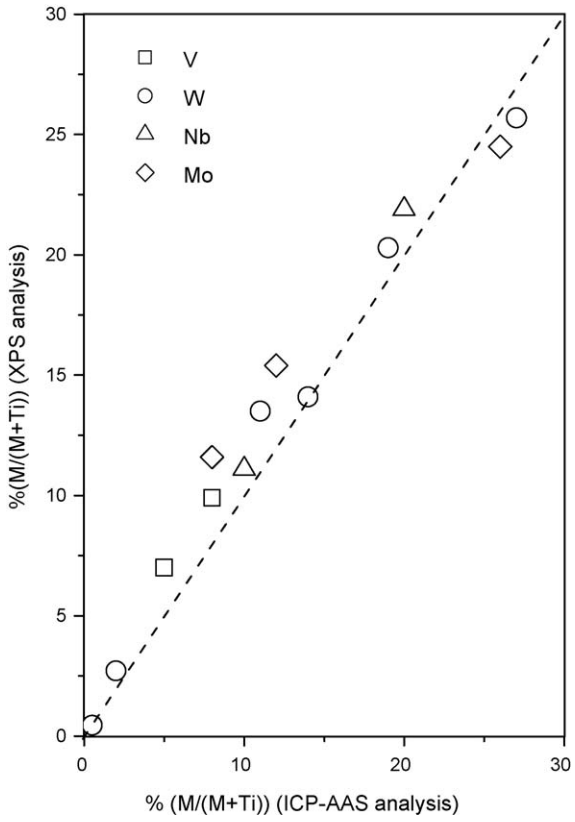


**Fig. 3.** XPS atomic concentration of heteroatom vs. heteroatom content of Ti–M materials.

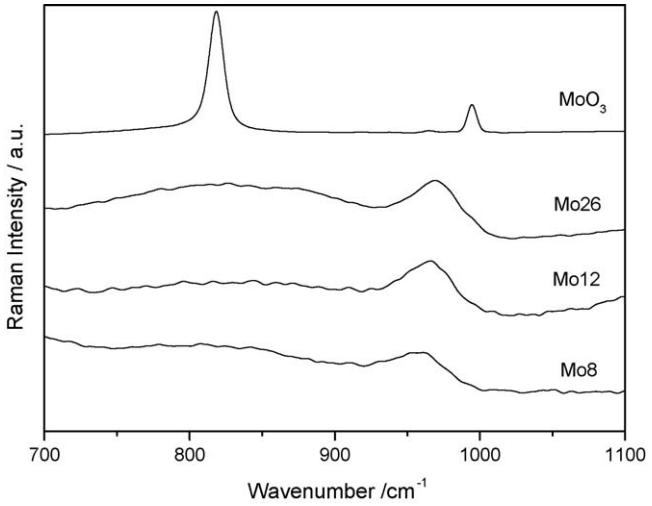


**Fig. 4.** Raman detail of the Mo–O–Mo and Mo═O species for Ti-Mo samples.

at substitutional positions of the anatase structure and the tendency of $V^{5+}$ to be at surface positions are intimately connected with their atomic radii ($V^{4+}/V^{5+}/Ti^{4+}$; 0.58/0.54/0.605 nm for sixfold coordination [37]).

Mo is the only metal to be significantly accumulated at the surface, even in a quantity exceeding that shown by V-containing samples above the corresponding solubility limit (Fig. 3). The Raman study (Fig. 4) of our samples provides evidence for the presence of small surface aggregates of Mo detecting the Mo═O (ca. 965 $cm^{-1}$) and Mo–O–Mo (broad contribution ca. 700–940 $cm^{-1}$) bands for samples with a content above 8 at. % [38]. The XPS binding energy reported in Table 2, 232.6 ± 0. 1 eV, indicates the presence of $Mo^{6+}$ species [36] in all cases, although a small contribution of $Mo^{5+}$ may be present in highly loaded samples. The presence of $Mo^{6+}$ at substitutional positions of the anatase network, likely favored by the corresponding atomic radius ($Mo^{6+}$, 0.59; $Ti^{4+}$, 0.605 nm for sixfold coordination [37]), seems dominant for all Mo-containing samples. According to the Mo–O–Mo Raman vibration, the surface $MO_x$ clusters are barely discernable for Mo12, but appeared as well developed 2D (two-dimensional) entities for the Mo26 sample. Note, in any case, that these are clearly surface cluster entities as no hint for Mo oxides are detected by XRD and the more sensitive Raman spectroscopy (with, in appropriate conditions, may detect a 0.1 wt.% of a surface V-, Nb-, Mo-, W-containing phase [38]).

Nb and W appear to form mixed oxides having larger solubility limits than V and also Mo. In the case of W, a study of the local arrangement of the heteroatom at the anatase structure was done in detail using EXAFS spectroscopy. Fig. 5 shows the $k^2$-weighted Fourier transform of the W $L_{III}$-edge and the corresponding fittings. Fitting results are summarized in Table 3. For our purposes, the main point of the fitting is the exclusive presence of Ti as first cationic neighbor of W and thus the presence of a single local arrangement, likely indicating the strong structural homogeneity of the Ti–W samples. Fig. 5B depicts however the decrease observed for the W–Ti shell coordination number above ca. 15 at.%, indicating the existence of two local arrangements. A single local arrangement where W ions have three Ti and one cation vacancy as first cationic coordination shell is observed up to 15 at.%. Above this cut-off point, a decrease of the Ti neighbors becomes evident and may indicate the accumulation of the heteroatom at grain frontiers and/surface, with a general decrease of the corresponding coordination numbers [24]. So, for W we unveiled the formation of

**Table 2**
Ti–M binding and band gap energies extracted from XPS and UV–vis, respectively.

| Sample | Binding energy (eV) | | | | | | Band gap energy (eV) |
|---|---|---|---|---|---|---|---|
| | Ti ($2p_{3/2}$) | O (1s) | V ($2p_{3/2}$) | Nb ($3d_{5/2}$) | Mo ($3d_{5/2}$) | W ($4d_{5/2}$) | |
| V1 | 458.2 | 529.4 | 517.2 | – | – | – | $2.9_5$ |
| V5 | 458.1 | 529.5 | 517.0 | – | – | – | $2.8_5$ |
| V8 | 457.8 | 529.2 | 516.5 | – | – | – | $2.8_5$ |
| Nb10 | 458.8 | 530.1 | – | 207.0 | – | – | 3.0 |
| Nb20 | 458.6 | 530.1 | – | 206.9 | – | – | 2.9 |
| Mo8 | 458.7 | 530.1 | – | – | 232.5 | – | 2.5 |
| Mo12 | 458.8 | 530.2 | – | – | 232.7 | – | 2.4 |
| Mo26 | 458.9 | 530.3 | – | – | 232.7 | – | 2.3 |
| W2 | 458.3 | 529.7 | – | – | – | 247.2 | 3.0 |
| W11 | 458.7 | 530.1 | – | – | – | 247.3 | $2.9_5$ |
| W14 | 459.0 | 530.6 | – | – | – | 247.5 | 2.9 |
| W19 | 459.2 | 530.5 | – | – | – | 247.7 | $2.7_5$ |
| W27 | 459.1 | 530.6 | – | – | – | 247.8 | $2.7_5$ |

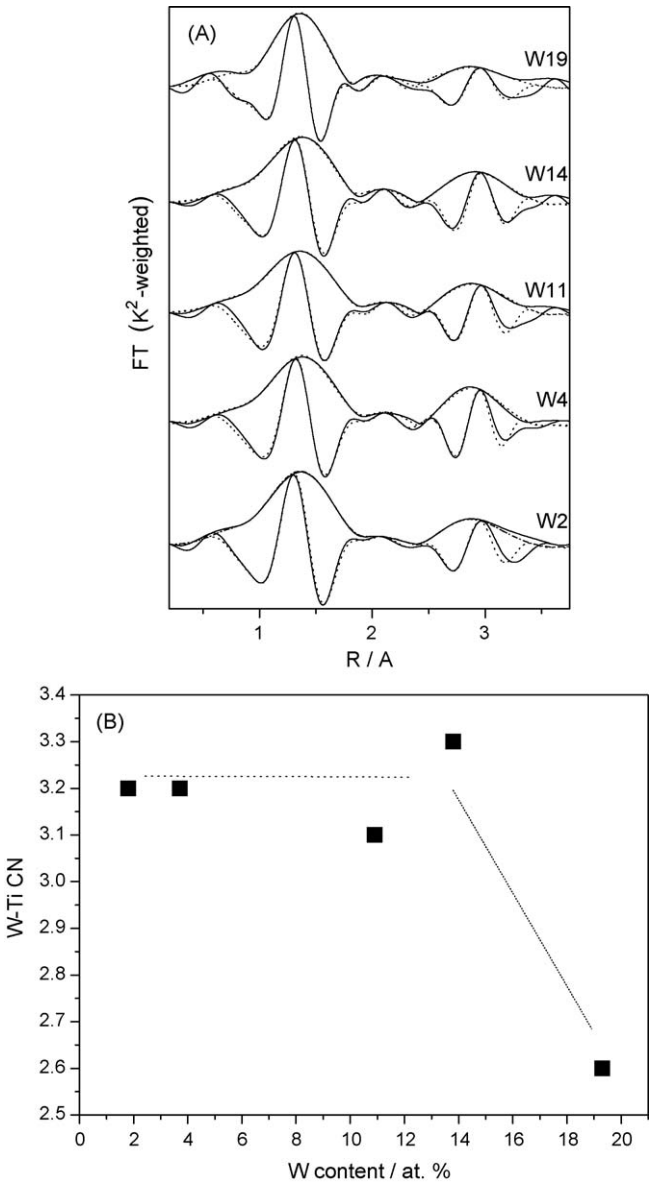


**Fig. 5.** (A) $k^2$-Weighted Fourier Transform of W $L_{III}$-edge EXAFS signals of Ti–W samples and (B) W–Ti coordination number as a function of the heteroatom content of the material.

Ti–W mixed oxides up to a heteroatom concentration close to 20 at.%. The large solubility region seems a consequence of the similar atomic radii of the $W^{6+}$ species detected by XPS (247.5 ± 0.3 eV [36]) and $Ti^{4+}$ ions (0.60 nm vs. 0.605 nm for sixfold coordination [37]) and the low likehood of having W–W contacts.

As mentioned Nb also appears to have a large solubility limit into the anatase structure as judged by the XPS (Fig. 3) and Raman (data not shown) study. This means that no Nb accumulation at surface positions is observed for the Ti–Nb samples. However, the analysis of the O 1s XPS peak (Fig. 6) provides conclusive evidence of Nb–O–Nb contacts within the anatase structure. Essentially, three different contributions are observed among the samples; the first is associated to oxygen lattice ions of the anatase network (ca. 530.0–530.5 eV), the second with surface hydroxyls at titania surfaces (ca. 530.9–531.5 eV [39]), and, in the case of the Ti–Nb series, a third at ca. 533.0–533.5 eV. This contribution can be associated with the presence of Nb-rich zones within the $TiO_2$–anatase structure as it approaches the characteristic binding

**Table 3**
W $L_{III}$-edge EXAFS fitting results for Ti–W mixed-metal oxides.

| Shell | $N$ | $R$(Å) | $\Delta\sigma$ ($10^3 \times$ Å$^2$) | $\Delta E_0$ (eV) |
|---|---|---|---|---|
| W2 | | | | |
| W–O | $4.55 \pm 0.3_5$ | $1.82 \pm 0.01$ | $10.3 \pm 0.4$ | $-4.9 \pm 1$ |
| W–O | $1.6 \pm 0.2$ | $2.61 \pm 0.01$ | $11.4 \pm 0.9$ | $-7.9 \pm 1$ |
| W–Ti | $3.2 \pm 0.3$ | $3.42_5 \pm 0.01$ | $9.1 \pm 0.6$ | $-8.0 \pm 1._5$ |
| W4 | | | | |
| W–O | $4.6 \pm 0.5$ | $1.83 \pm 0.01$ | $12.0 \pm 0.4$ | $-4.9 \pm 1$ |
| W–O | $1.8 \pm 0.2$ | $2.62 \pm 0.01$ | $10.5 \pm 1.2$ | $-4.7 \pm 1$ |
| W–Ti | $3.2 \pm 0.2_5$ | $3.39_5 \pm 0.02_5$ | $5.5 \pm 0.6$ | $-11.0 \pm 1._5$ |
| W11 | | | | |
| W–O | $4.35 \pm 0.4$ | $1.82 \pm 0.01$ | $12.0 \pm 0.4$ | $-5.0 \pm 1$ |
| W–O | $1.5_5 \pm 0.3$ | $2.61_5 \pm 0.01$ | $7.5 \pm 1.5$ | $-7.9 \pm 1$ |
| W–Ti | $3.1 \pm 0.2$ | $3.41_5 \pm 0.02$ | $8.0 \pm 0.9$ | $-8.5 \pm 1$ |
| W14 | | | | |
| W–O | $4.1 \pm 0.3_5$ | $1.82 \pm 0.01$ | $10.4 \pm 0.4$ | $-4.8 \pm 1$ |
| W–O | $1.6 \pm 0.1$ | $2.60 \pm 0.01$ | $7.7 \pm 0.6$ | $-7.1 \pm 1$ |
| W–Ti | $3.3 \pm 0.3$ | $3.42_5 \pm 0.01$ | $8.0 \pm 0.5$ | $-7.2 \pm 1._5$ |
| W19 | | | | |
| W–O | $3.25 \pm 0.3_5$ | $1.81 \pm 0.01$ | $6.1 \pm 0.4$ | $-5.0 \pm 1$ |
| W–O | $1.7 \pm 0.2$ | $2.54 \pm 0.01$ | $9.1 \pm 0.4$ | $-10.0 \pm 1$ |
| W–Ti | $2.6 \pm 0.3$ | $3.40 \pm 0.01$ | $8.7 \pm 1.5$ | $-8.5 \pm 1._5$ |

energy of the single oxide at surface positions [40] and appears in samples where absence of Nb-only phases have been demonstrated using XRD–Rietveld and the most sensitive Raman spectroscopy. Such a third contribution is also weakly observed in Ti–Mo (Fig. 6) but is certainly of much less importance than in the Ti–Nb case and associated with Mo-rich zones of rather limited size [41,42], previously detected by Raman at the surface of the material (Fig. 4). According to XPS, Table 2, Nb species display a 207.0 ± 0. 1 eV binding energy, somewhat lower to the characteristic $Nb^{5+}$ species in the $Nb_2O_5$ oxide matrix but well above $Nb^{4+}$ [36]. This is likely an effect of the coordination change which may be inferred from the presence of a hetero-ion having a larger ionic radius ($Nb^{5+}$, 0.64 nm; $Ti^{4+}$, 0.605 nm for sixfold coordination) at $TiO_2$–anatase substitutional positions suffering a modest lowering of symmetry and/or local disordering to accommodate a bigger cation. So, although Nb seems to accommodate its valence electron distribution to be at the anatase network, it appears that there is always Nb-rich local zones which are essentially located at bulk or near surface but no surface positions.

So, the structural study shows that we have a growing solubility limit of $V \ll Mo < Nb \approx W$ into the anatase structure but, in addition, structural differences among Ti–M samples concerning local order. As summarized in Table 4, we found that V and W show a single local arrangement around the heteroatom with exclusive presence of Ti (and cation vacancies in the case of W) as first cationic neighbor. Mo seems also to follow that trend but with tendency to be at the surface. Nb displays a large solubility limit but with the concomitant presence of Nb-rich local arrangements within the anatase structure. The different local arrangements are reflected in the long-range order. As depicted in Fig. 7, we can only detect changes in anatase tetragonality for Ti–V and Ti–W above the corresponding solubility limits. In contrast, Mo mainly shows changes in tetragonality, similar to Ti–W/Ti–V when $WO_x$/$VO_x$ clusters are at the surface of nanosized titania particles. It thus appears that the limited primary particle size of the anatase allows its structural alteration by $MO_x$ surface entities. The alteration of the anatase structure appears maximum at Ti–Nb samples and not only the tetragonality but also the cell volume need to vary to accommodate the alien cation. As a result, we found that V and W seem to produce highly homogeneous anatase-type mixed

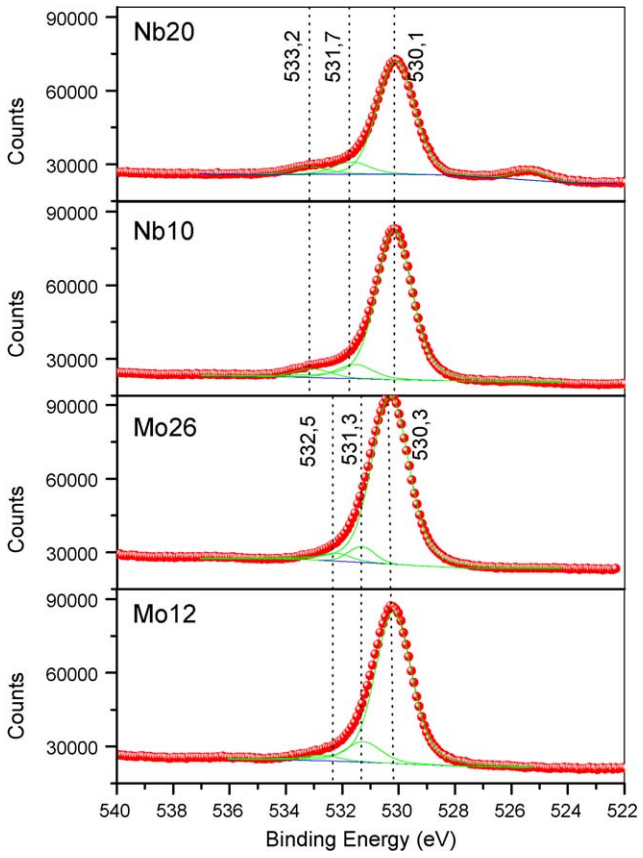


**Fig. 6.** O 1s XPS signals for Ti–Nb and Ti–Mo samples.

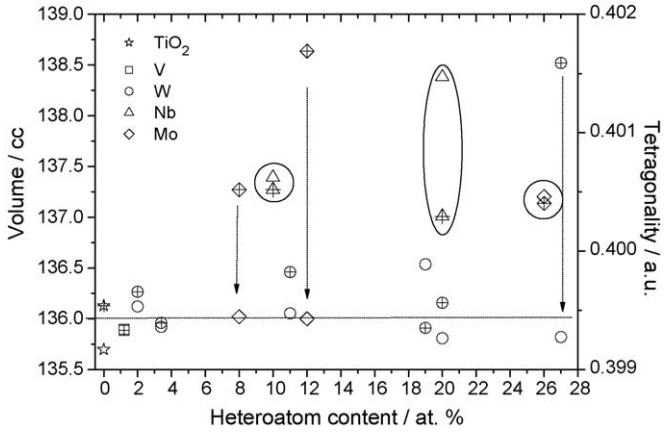


**Fig. 7.** Anatase cell parameters from XRD–Rietveld analysis. Dashed lines are only a guide for the aids. Open symbols: cell volume; crossed symbols: tetragonality.

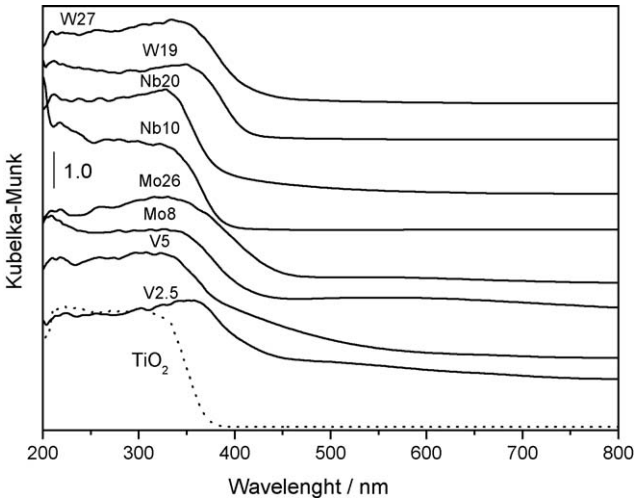


**Fig. 8.** UV-spectra of selected Ti–M materials.

oxides with well defined local order and minimum disturbance of the anatase long-range order, while Mo and particularly Nb alter the anatase structure in a way which has both local (e.g. presence of $MO_x$ clustering) and long-range (tetragonality and/or cell volume changes) structural effects.

To analyze the electronic consequences of such structural changes, the UV–vis spectra of the Ti–M were obtained. Fig. 8 plots those spectra of the more interesting (around the solubility limit) samples. Two main physico-chemical features can be investigated using these plots. First, the presence of unoccupied localized electronic states giving electronic transitions in the spectra are evident in the Ti–V case and less significantly in the Ti–Mo series and the Nb20 sample. Ti–V localized states have been previously analyzed with the help of UV–vis spectroscopy; essentially, Fig. 8 provides evidence of $V^{4+}$ d–d transitions around 550 nm and of $V^{5+}$ (vanadates) excitations around 450 nm [11]. Ti–Mo samples also displayed a broad band centered at ca. 550 nm containing contributions ascribable to $Mo^{5+}$–$Mo^{6+}$ intervalence charge transfer as well as $Mo^{5+}$ d–d transition [43]. This band seems to change its center as the Mo content grows but this effect is only of moderate magnitude, in agreement with XPS results that indicate a residual $Mo^{5+}$ fraction. In the case of the Ti–Nb series, only the highest loading sample displays an Urbach-type tail after the characteristic charge transfer band, which might be attributed to the presence of Nb-rich zones as earlier discussed.

The second main feature extracted from the UV–vis study concerns the band gap behavior as a function of the M heteroatom nature and concentration (Table 2). While bulk $TiO_2$ is an indirect semiconductor, nanostructured materials can be direct ones [44,45]. Band gaps values were estimated from the absorbance

**Table 4**
Main structural and electronic properties of the anatase-type phase of Ti–M materials.

| Doping metal | Solubility limit (at.%) | Cell tetra/vol.[a] | M local neighbor atom | Bulk/surface ox. state and coordination | Band gap/mid gap states[a,b] |
|---|---|---|---|---|---|
| V | 2 | −/− | Ti | $^{4+2}$V(IV)/$^{5}$V(V) | r.s./− |
| Mo | >12 | +/− | Ti, Mo | $^{4+2}$Mo(VI)/$^{6}$Mo(VI)[c] | r.s./+ |
| Nb | 20 | +/+ | Nb, Ti | $^{4+2+1}$Nb(VI)/− | s.s./+ |
| W | 20 | −/− | Ti | $^{4+2}$W(VI)/$^{5}$W(VI) | r.s./− |

Data exclusively for Ti–M mixed oxides below the corresponding solubility limits.
[a] +, changes from $TiO_2$; −, absence of changes.
[b] r.s. = red shifted band gap with respect to that of $TiO_2$ oxide; s.s. = small red shift.
[c] Mo(V) species detected below 5%.

spectra using both types of analysis (i.e. for direct and indirect transitions); the trends observed were the same in both cases. In Table 2 we therefore show the calculated indirect band gap energy. The ca. 3.1 eV value obtained for nanostructured anatase–$TiO_2$ agrees well with data previously reported [5,44]. Trends in Table 2 showed decreasing behaviors for all Ti–M systems. However, this decrease is somehow moderate (0.2 eV) for Ti–V, in accordance of the moderate concentration of V present into the $TiO_2$–anatase structure and reaches a constant value after the solubility limit. It should be mentioned that the error in the band gap estimation of Ti–V samples is however large due to the presence of bands associated to localized states at ca. 450 nm, close to the band gap [11]. A small band gap decrease is surprisingly observed in the case of Ti–Nb while more significant changes are detected for the Ti–Mo and Ti–W series.

So, discarding atomic-like d–d transitions which would not play a significant role in generating charge carriers, we see a general decrease of the band gap of the anatase structure which seems to have an intensity behavior $V < Nb < W \ll Mo$. The power of V is strongly limited by its low solubility limit into the anatase structure although for low concentrations seems to drive to a relative important decrease with respect to other M cations. The more important decrease of the band gap occurs with Mo. As summarized in Table 4, Nb and Mo also generate the presence of localized states giving absorption under visible light energies. This seems very clear for the Ti–Mo series and appears also evident for the Nb20 sample. Presence of such states clearly correlates with M-rich local arrangements (either at the surface, Mo, or bulk, Nb) and seems to negatively influence photo-activity (Fig. 1), likely by an enhancement of the recombination process.

## 4. Conclusions

In summary, the present report establishes a link between structure and photo-activity; the extensive structural/electronic analysis carried out suggests that the existence of highly homogeneous Ti–M mixed oxides (both at local and long-range levels) with electronic properties exclusively leading to a decrease of the band gap would drive to efficient photocatalysts under visible-light excitation. In our case, this occurs with V and W; the low solubility limit of V limits its usefulness and would lead to the conclusion that, within our preparation method and considering anatase-type Ti–M binary oxides, W is the optimum choice to produce Ti-based mixed oxides with optimum photocatalytic activity under sunlight-type excitation. The physico-chemical characterization also allows to speculate that a combination of V with high-solubility doping cations like W may boost photo-activity and would yield anatase-type Ti–V–M ternary oxides with enhanced performance with respect to the binary materials described here.

## Acknowledgements

A.K. thanks the CSIC for a I3P post-doctoral grant. Financial support by the projects CTQ-2007-60480/BQU, and P06-FQM-1406 are fully acknowledged.

## References

[1] M.R. Hoffman, S.T. Martin, W. Choi, D.W. Bahneman, Chem. Rev. 95 (1995) 69.
[2] A.J. Maira, J.M. Coronado, V. Augliaro, K.L. Yeung, J.C. Conesa, J. Soria, J. Catal. 2002 (2001) 413.
[3] K.L. Yeung, S.T. Yau, A.J. Maira, J. Soria, P.L. Yue, J. Catal. 219 (2003) 107.
[4] G. Colón, C. Belver, M. Fernández-García, in: J.A. Rodríguez, M. Fernández-García (Eds.), Synthesis, Properties, and Applications of Oxide Nanomaterials, John Wiley & Sons, New Jersey, 2007 (Chapter 17).
[5] M. Fernández-García, A. Martínez-Arias, J.C. Hanson, J.A. Rodriguez, Chem. Rev. 104 (2004) 4063.
[6] M.M. Cohen, Introduction to the Theory of Semiconductors, Gordon, Amsterdam, 1999.
[7] N.I. Al-Salim, S.A. Bagshaw, A. Bittar, T. Kemmit, A.J. McQuillan, A.M.J. Mills, M.J. Ryan, J. Mater. Chem. 10 (2000) 2358.
[8] V. Luca, S. Thomson, R.F. Howe, J. Chem. Soc., Faraday Trans. 93 (1997) 2195.
[9] M. Anpo, M. Takeuchi, J. Catal. 216 (2003) 505.
[10] J.J. Shyre, M.R. DeGrure, J. Am. Chem. Soc. 127 (2005) 12736.
[11] A. Kubacka, A. Fuerte, A. Martínez-Arias, M. Fernández-García, Appl. Catal. B 74 (2007) 26.
[12] L. Depero, L. Sagaletti, B. Allieri, E. Bontempi, L.E. Marino, M. Zachii, J. Cryst. Growth 198 (1999) 516.
[13] A. Kubacka, M. Fernández-García, G. Colón, J. Catal. 254 (2008) 272.
[14] J.A. Wang, R. Limas-Ballesteros, T. López, A. Moreno, R. Gómez, O. Novaro, X. Bokhim, J. Phys. Chem. B 105 (2001) 9692.
[15] J. Zhu, F. Chen, J. Zhang, H. Chen, M. Anpo, J. Photochem. Photobiol. A 180 (2006) 196.
[16] C. Adán, A. Bahamonde-Santos, M. Fernández-García, A. Martínez-Arias, Appl. Catal. B 72 (2007) 11.
[17] J.C. Yu, J. Lin, R.W.M. Kwok, J. Phys. Chem. B 102 (1998) 5094.
[18] Y. Huang, Z. Zheng, Z. Ali, L. Zhang, X. Fan, Z. Zou, J. Phys. Chem. B 110 (2006) 19323.
[19] M.D. Hernández-Alonso, J.M. Coronado, B. Bachiller-Baeza, M. Fernández-García, J. Soria, Chem. Mater. 19 (2007) 4283.
[20] V. Guidi, M.C. Carotta, M. Ferroni, G. Martinelli, M. Sacerdoti, J. Phys. Chem. B 107 (2003) 120.
[21] A. Mattson, M. Leideburg, K. Larsson, G. Westin, L. Osterlund, J. Phys. Chem. B 110 (2006) 1210.
[22] M.S. Jeon, W.S. Yoon, H. Joo, T.K. Lee, H. Lee, Appl. Surf. Sci. 165 (2000) 209.
[23] A. Fuerte, M.D. Hernández-Alonso, A.J. Maira, A. Martínez-Arias, M. Fernández-García, J.C. Conesa, J. Soria, G. Munuera, J. Catal. 212 (2002) 1.
[24] M. Fernández-García, A. Martínez-Arias, A. Fuerte, J.C. Conesa, J. Phys. Chem. B. 109 (2005) 6075.
[25] X.C. Dai, H.Y. Xiao, W.S. Li, Y.Q. Na, Appl. Catal. A 290 (2005) 25.
[26] V. Luca, M.G. Backford, K.S. Finnie, P.J. Evans, M. James, M.J. Lindsay, M. Skyllas-Kazacos, P.R.F. Barnes, J. Phys. Chem. C 111 (2007) 18479.
[27] N. Consuelo, F.S. García-Einschalg, R.J. Candal, M. Jobbagy, J. Phys. Chem. C 112 (2008) 1094.
[28] F.R. Sensato, R. Custodio, E. Longo, A. Beltrán, J. Andrés, J. Catal. Today 85 (2003) 145.
[29] F. Fresno, D. Tudela, J.M. Coronado, M. Fernández-García, A. Hungría, J. Soria, Phys. Chem. Chem. Phys. 8 (2006) 2421.
[30] H. Choi, E. Stathatos, D. Dionysiou, Thin Solid Films 510 (2006) 107.
[31] G.K. Willianson, W.H. May, Acta Metall. 1 (1953) 22.
[32] S. Krustev, Bull. Chem. Commun. 30 (1998) 408.
[33] K.V. Klementev, J. Phys. D: Appl. Phys. 34 (2001) 209.
[34] A.J. Maira, K.L. Yeung, J. Soria, J.M. Coronado, C. Belver, C.Y. Lee, V. Augugliaro, Appl. Catal. B 29 (2001) 327.
[35] A. Vittadini, M. Casarin, M. sambi, A. Selloni, J. Phys. Chem. B 109 (2005) 21766.
[36] C.D. Wagner, W.M. Riggs, L.E. Davis, J.F. Moulder, in: G.E. Muilenber (Ed.), Handbook of X-ray Photoemission Spectra, Perkin–Elmer, Minnesota, 1976.
[37] R.D. Shanon, Acta Crystallogr. A 32 (1976) 751.
[38] Y. Chen, I.E. Wachs, J. Catal. 217 (2003) 468.
[39] G. Colón, M.C. Hidalgo, G. Munuera, I. Ferino, M.G. Cutrufello, J.A. Navío, Appl. Catal. B 63 (2006) 45.
[40] R. Wojcieszak, A. Jasik, S. Monteverde, M. Ziolek, M.M. Vetar, J. Mol. Catal. A: Chem. 256 (2006) 225.
[41] A. Katrib, A. Benadda, U.W. Sobczak, G. Maire, Appl. Catal. A: Gen. 242 (2003) 31.
[42] C.V. Ramana, V.V. Atuchin, V.G. Kesler, V.A. Kochubey, L.D. Pokrovsky, V. Shutthanadan, U. Becker, R.C. Ewing, Appl. Surf. Sci. 253 (2007) 5368.
[43] M. Dieterle, G. Weinberg, G. Mesta, Phys. Chem. Chem. Phys. 4 (2002) 812.
[44] N. Serpone, D. Lawless, V. Khairutdinov, J. Phys. Chem. 98 (1995) 16646.
[45] K.M. Reddy, S.V. Mamorama, A.M. Reddy, Mater. Chem. Phys. 78 (2002) 239.